Nanoscale

Cite this: *Nanoscale*, 2011, **3**, 5026

www.rsc.org/nanoscale

PAPER

In vitro detection of superoxide anions released from cancer cells based on potassium-doped carbon nanotubes–ionic liquid composite gels

Xiao-Rong Li, Bo Wang, Jing-Juan Xu* and Hong-Yuan Chen

Received 5th August 2011, Accepted 10th September 2011
DOI: 10.1039/c1nr11025j

A newly developed electrochemical biosensor for the determination of superoxide anions ($O_2^{\cdot-}$) released from cancer cells using potassium-doped multi-walled carbon nanotubes (KMWNTs)–1-butyl-3-methylimidazolium hexafluorophosphate ([BMIM]PF_6) ionic liquid composite gels is demonstrated. The KMWNTs–[BMIM]PF_6 can electrocatalyze oxygen reduction to generate a strong current signal in neutral solution. Compared with KMWNTs without [BMIM]PF_6 or MWNTs–[BMIM]PF_6 composites, the KMWNTs–[BMIM]PF_6 can enhance the oxygen reduction peak current by 6.2-fold and 2.8-fold, which greatly increases the detection sensitivity of oxygen. Then, $O_2^{\cdot-}$ biosensors are fabricated by mixing superoxide dismutase (SOD) in the KMWNTs–[BMIM]PF_6 gels *via* monitoring oxygen produced by an enzymic reaction between SOD/$O_2^{\cdot-}$ without the help of electron mediators. The resulting biosensors show a linear range from 0.04 to 38 μM with a high sensitivity of 98.2 μA mM^{-1}, and a lower detection limit of 0.024 μM. The common interferents such as hydrogen peroxide (H_2O_2), ascorbic acid (AA), uric acid (UA), and metabolites of neurotransmitters, do not interfere with the detection of $O_2^{\cdot-}$. The proposed biosensor is tested to determine $O_2^{\cdot-}$ *in vitro* and from liver cancer and leukemia cells and shows good application potential in biological electrochemistry.

Introduction

Reactive oxygen species (ROS), including the superoxide anion ($O_2^{\cdot-}$), hydrogen peroxide (H_2O_2), the hydroxyl radical (OH˙) and peroxynitrite ($ONOO^-$), and so on, lead to oxidative damage to lipids, proteins and nucleic acids, resulting in mutagenesis and cell death.[1] $O_2^{\cdot-}$, the primary component of the so-called ROS, is generated as a reduced intermediate of molecular oxygen in significant quantities in a variety of biological systems. Under normal physiological conditions, $O_2^{\cdot-}$ is produced at a rate that is matched by the capacity of tissue to catabolize them, thus holding a rather low and undetectable endogenous physiological concentration. However, increases in the activity of $O_2^{\cdot-}$ occurring in response to traumatic brain injury,[2,3] ischemia-reperfusion and hypoxia, which exceeds the body's natural ability to deal with the potentially cytotoxic species, may be involved in the etiology of aging, cancer, and progressive neurodegenerative diseases such as Parkinson's disease.[4–10] Additionally, $O_2^{\cdot-}$ can easily form OH˙ in the presence of transition metal ions such as Fe^{2+} and Cu^{2+} and react with NO to produce $ONOO^-$,[11–15] which have also been implicated in the pathogenesis of atherosclerosis and neurodegenerative diseases. As a consequence, $O_2^{\cdot-}$ is of great significance in the determination of cellular damage, and a selective and sensitive method for durable and reliable measurement of $O_2^{\cdot-}$ is essential and very useful for facilitating investigations on free-radical biochemistry and the pathology and physiology of diseases relevant to ROS.

Superoxide dismutase (SOD) has been well addressed for the dismutation of $O_2^{\cdot-}$ to O_2 and H_2O_2 with strong activity and great specificity, and this strategy was recently used to develop $O_2^{\cdot-}$ sensors.[16–20] Most of the sensors are based on monitoring the oxidation current of H_2O_2 produced from $O_2^{\cdot-}$ dismutation catalyzed by SOD. In these sensors, high potentials (>0.6 V *versus* SCE) which usually cause the simultaneous oxidation of some coexisting electroactive species in biological samples, *e.g.*, AA and UA, are required. More importantly, H_2O_2 is a metabolite of the degradation of $O_2^{\cdot-}$ as well as a product from the enzymatic reaction of endogenous oxidases such as monoamine oxidase and L-amino acid oxidase.[4,11,12] Thus, it is necessary to differentiate the signals of H_2O_2 produced by SOD catalytic dismutation of $O_2^{\cdot-}$ from H_2O_2 endogenously present in biological systems. The interference from the coexisting electroactive species and endogenous H_2O_2 greatly limit the practical applications of sensors determining $O_2^{\cdot-}$ in biological systems.[4,21,22] Several approaches have been developed to try to solve the interference effects and overlap signals from endogenous H_2O_2 to enhance the selectivity for these types of sensors: a H_2O_2-impermeable Teflon membrane,[23] combination with horseradish peroxidase,[24] the entrapment of SOD between two membranes,[25] and the incorporation of SOD in a polypyrrole film[26,27] or the use of a poly-m-phenylenediamine membrane,[28] but the sensitivity and the response rate decreased. At this point, a two-channel

State Key Laboratory of Analytical Chemistry for Life Science, School of Chemistry and Chemical Engineering, Nanjing University, Nanjing, 210093, P. R. China. E-mail: xujj@nju.edu.cn; Fax: (+86)25-8359-7924

sensor, which is capable of simultaneous detection of $O_2^{\cdot-}$ and H_2O_2, was proposed.[16] However, the difference in amperometric response of two independent electrodes to H_2O_2 makes it difficult to obtain a net response of $O_2^{\cdot-}$ at the sensor for both $O_2^{\cdot-}$ and H_2O_2. In addition, the third-generation biosensors for $O_2^{\cdot-}$ based on direct electron transfer of proteins have paved an elegant way to detect $O_2^{\cdot-}$ due to excellent selectivity and high sensitivity, in which SOD were widely employed, but direct contact between enzymes and electrodes often leads to significant structural and/or functional changes of the enzymes.[10] To challenge these key analytical problems, enzymatically generated oxygen can be monitored based on its reduction because the electrochemical reduction of oxygen that occurred at a relatively negative potential does not give rise to interference from those anodic interfering species like UA, AA. More noteworthy, the reductive potential of H_2O_2 is commonly more negative than that of oxygen;[10] therefore, it is very easy to detect oxygen free from the interference of H_2O_2 at those negative potentials, regardless that H_2O_2 exists extensively in the biological system and is associated with the formation of H_2O_2. Moreover, it is also very easy to eliminate the interference from oxygen in biological systems by bubbling nitrogen or other inert gases for the determination of $O_2^{\cdot-}$ *in vitro*. However, electrocatalytic reduction of oxygen at conventional electrodes usually suffers from poor kinetics. So it is very significant to exploit a novel material with superior performance for the reduction of oxygen as well as develop a highly selective biosensor with micromolar or even nanomolar sensitivity to provide quantitative information on $O_2^{\cdot-}$ concentrations for tracking the role that $O_2^{\cdot-}$ plays in physiological and pathological processes.

Recently, chemical doping is a leading potential strategy to enrich free charge-carrier densities and enhance the electrical or thermal conductivities in carbon materials.[29–31] Many studies have demonstrated the achievements of chemical doping of carbon nanotubes.[32–40] Among the numerous potential dopants, K is considered as an excellent element for the chemical doping of carbon nanotubes with a modified structure or morphology, resulting in changed electrical, mechanical, and chemical properties of carbon nanotubes.[32,33,41] Moreover, K-doped multi-walled carbon nanotubes (KMWNTs) have demonstrated that K doping could enhance the biocompatibility and sensitivity of carbon nanotubes in biosensing applications. As with the MWNTs,[42] the KMWNTs typically assemble to give bundles, which are heavily entangled with one another to form agglomerates. These structural aspects give KMWNTs relatively poor mechanical and electroconductive properties. To modify their chemical and physical properties, one could expect much greater performance of KMWNTs on composite materials. Organic cations, which potentially interact with π-electronic compounds through so-called "cation–π" interactions are focued.[43] At this point, ammonium ion-based molten salts[44,45] have attracted great interest, because they are fluid at room temperature with non-volatility, in sharp contrast with ordinary organo- and hydrogels, are highly stable and can retain their physical properties, thus can be directly used as media for processing. We found that the room-temperature ionic liquid (RIL) of imidazolium ions,[46] 1-butyl-3-methylimidazolium hexafluorophosphate ([BMIM]PF_6), upon being ground with KMWNTs, forms physical gels (bucky gels). More importantly, the ionic liquid has great promise in green chemistry applications and in electrochemical applications, particularly, because of its high stability, high electrochemical conductivity, and very low vapor pressure.[46–48] Also it has wide solubility which is quite helpful for the dispersion of KMWNTs. In addition, high biocompatibility and exchangeability of the counter-anions in RIL, *e.g.*, with negatively charged enzymes, are much favorable for further immobilization of biomolecules.

As bucky gels appear to possess high potential utilities in materials sciences, we employed [BMIM]PF_6 and found that finely dispersed KMWNTs can cause better mechanical and electroconductive properties of the materials. In the present work, we report detailed accounts of the preparation, microstructures, and electroconductive properties of the KMWNTs–[BMIM]PF_6 bucky gels. The gels as oxygen reduction reaction catalysts show a strong reduction signal in neutral solution. Thus they could be employed as highly selective oxygen sensors in a more positive potential (−0.3 V) than non-modified electrodes. Furthermore, by utilizing the excellent electroreduction property toward oxygen, we have developed a highly specific biosensor for $O_2^{\cdot-}$ based on the SOD-modified KMWNTs–[BMIM]PF_6 composite gels. This biosensor exhibited ease of fabrication and excellent performance, such as fast response, good stability and reproducibility, and low detection limit. More importantly, the biosensor has great benefits for the detection of $O_2^{\cdot-}$ with a relatively high selectivity, avoiding not only some coexisting interferences like AA, UA, and metabolites of some neurotransmitters but also more noteworthy interference, H_2O_2. The developed biosensor was used to measure $O_2^{\cdot-}$ released from living cells, which could be very important as there is increasing evidence that $O_2^{\cdot-}$ released from biological systems may have a role in the etiology of aging, cancer, and progressive neurodegenerative diseases such as Parkinson's disease.[5–8]

Experimental section

Materials

Multi-walled carbon nanotubes (MWNTs, 95%, $d < 10$ nm) were provided by Shenzhen Nano-tech port Co. (China). 1-butyl-3-methylimidazolium hexafluorophosphate ([BMIM]PF_6, 99%) was purchased from Shanghai Cheng Jie Chemical Co. Ltd. (China). Superoxide dismutase (SOD, EC 1.15.1.1) from bovine erythrocytes was commercially available from Sigma (USA). Potassium superoxide (KO_2), potassium (K), phenanthrene, 1,2-dimethoxyethane (1,2-DME), dimethylsulfoxide (DMSO), glucose (GC), L-ascorbic acid (AA), uric acid (UA), lactic acid (LA), glutamic acid (GA) and lipopolysaccharide (LPS) were obtained from Sigma-Aldrich (USA). Acridine orange (AO) and ethidium bromide (1% w/v, EB) were purchased from Amresco (USA). The $O_2^{\cdot-}$ solution was obtained from a 0.01 M stock solution of KO_2, which was prepared by adding 1.41 mL of DMSO (stored together with a 4 Å molecular sieve (Roth, Karlsruhe, Germany) to 1.0 mg KO_2, sonicating for 5 min and then putting an additional 4 Å molecular sieve in the solution to exclude H_2O. All other chemical materials were of analytical grade and used without further purification in experiments. Ultra-pure water which was obtained from a Milli-Q water

purifying system was used for the preparation of all aqueous solutions.

Apparatus

Transmission electron microscopy (TEM) micrographs were obtained on a JEOL JEM-3011 transmission electron microscope. X-ray photoelectron spectroscopy (XPS) measurements were performed with an Ultra Axis spectrophotometer (Kratos Analytical Ltd., Manchester, UK) equipped with a monochromatic Al Kα source operated at 150 W. Resonance Raman spectra were measured on a LabRAM HR 800 Raman spectrophotometer (Jobin Yvon, France). Fluorescence microimagings were recorded on a DMIRE2 inverted fluorescence microscope (Leica, Germany) equipped with a DP71 CCD (Olympus, Japan). Electrochemical measurements were performed on a computer-controlled electrochemical analyzer (CHI 660C, Shanghai Chenhua Apparatus, China). Linear sweep voltammetry and amperometric current–time curve measurements were carried out in 0.1 M phosphate buffer solution (PBS, pH 7.4) and cyclic voltammetry measurements were carried out in 0.1 M KCl solution containing 5.0 mM $K_3[Fe(CN)_6]/K_4[Fe(CN)_6]$, respectively, at room temperature (25 $\pm$ 2 °C) using a conventional three-electrode system with a glassy carbon electrode (GCE) as a working electrode, a platinum foil as an auxiliary electrode, and a saturated calomel electrode (SCE) as a reference electrode.

Synthesis of KMWNTs

The KMWNTs were synthesized according to chemical K-doping at room temperature.[32,33] In brief, MWNTs were pretreated by sonicating in a mixture of concentrated sulfuric acid–nitric acid (3: 1, v/v) for about 4 h. The treated MWNTs were filtered and washed with ultra-pure water, and then dried in a vacuum at 60 °C. After that, the phenanthrene/K solution complex was made by reacting K (200 wt% to MWNTs) with 0.2 M of phenanthrene (98%) in 20 mL of 1,2-DME (99.5%) solution. Then, the treated MWNTs (20 mg) were added to the phenanthrene/K solution complex for the K-doping into MWNTs. Finally, the reaction was conducted for 48 h with stirring using a magnetic bar at 500 rpm at room temperature. The resulting product was thoroughly washed several times with ethanol, and then dried at 60 °C under air atmosphere.

Preparation of modified electrodes

Glassy carbon electrodes (GCE, d = 3 mm, *ca.* 0.07 cm^2) were abraded with fine SiC paper and polished to a mirror-like surface with 1.0 and 0.3 μm alumina slurry, and then sonicated in water and absolute ethanol for 2 min, respectively, and dried at room temperature. KMWNTs (2 mg) were suspended in a RIL ([BMIM]PF_6) (0.4 mL), and the mixture was ground with an agate mortar for 15 min, where the suspension gradually turned into a glossy, black paste. The resulting paste was centrifuged at 10 000 rpm for 30 min, followed by the removal of excess liquid, to isolate a gel phase. Then, the KMWNTs–[BMIM]PF_6 composite gels were coated on the pretreated GCE by rubbing the electrode over the gels. The superoxide biosensor was prepared using 0.5 mg of SOD for every 2 mg of the composite material. Here, because the isoelectric point, I_p of SOD is 5.5, it is net negative at pH > I_p, and would exchange the PF_6^- anion on KMWNTs–[BMIM]PF_6 to SOD, which allows a more general electrostatic interaction between [BMIM]PF_6 functionalized KMWNTs and SOD. Briefly, the composite gels were prepared first and then the enzyme was added, and the gels were mixed for another 15 min. Finally, the KMWNTs–[BMIM]PF_6–SOD composites were coated on the pretreated GCE by rubbing the electrode over the hybrid composites. To obtain a homogeneous thin film, the coating was further smoothed with a spatula and the modified amount was controlled to 0.5 mg by weighing. Additionally, the modified electrodes were rinsed carefully with ultra-pure water prior to each measurement.

Cell line and culture

The concentration of $O_2^{\cdot-}$ released from human leukemia (HL-60) and liver cancer (SMMC-7721) cells was determined using the modified electrode. Cells were grown at 37 °C in RPMI 1640 medium (GIBCO) supplemented with 10% (v/v) fetal bovine serum (FBS, GIBCO), 60 μg mL^{-1} penicillin, and 100 μg mL^{-1} streptomycin in a 5% CO_2 environment. After 24 h, the cells were collected and separated from the medium by centrifugation at 1000 rpm for 5 min and then washed twice with sterile PBS (pH 7.4). The sediment was resuspended in PBS to obtain a homogeneous cell suspension at a certain concentration. The cell number was determined using a Petroff Hausser cell counter (USA). For $O_2^{\cdot-}$ detection, cells were treated with 50 ng mL^{-1} of LPS for a period of 0–96 h. Then, cells (10^5 cells cm^{-2}) were centrifuged and the cultured supernatants were collected and used for $O_2^{\cdot-}$ analysis by bubbling nitrogen to remove oxygen. Next, the recovery measurements were carried out according to the following procedures. The two different cells samples (HL-60 and SMMC-7721 cells supernatants) were prepared, and certain amounts of $O_2^{\cdot-}$ (0.2, 0.3 and 0.6 μM) were added. The concentrations of $O_2^{\cdot-}$ in the total sample mixtures were measured by the amperometric current–time curve method by comparing the current values to a calibration curve. Recovery was then calculated by the ratio of measured amount and added amount. Each sample was analyzed in quintuplicate.

Results and discussion

Characterization of the KMWNTs and KMWNTs–[BMIM]PF_6 composite gels

KMWNTs have been synthesized according to chemical K-doping at room temperature. XPS is a powerful tool to identify the states of the elements in bulk material. According to the analysis of binding energy (BE) values, we can confirm the nature of the binding between carbon and potassium. As shown in Fig. 1A, no K peaks are observed for MWNTs. However, K peaks in the spectra of KMWNTs are observed at BE = 293.2 eV (K $2p_{3/2}$) and 296.0 eV (K $2p_{1/2}$) (Fig. 1B). The two peaks correspond to a spin–orbit split doublet, which can be ascribed to the K oxides and cations, respectively.[33,49,50] Thus, only one K species is observed in the metal-doping process. The highly reactive K atoms can readily react with the surface migrated oxygen from the bulk of the MWNTs to form an oxidized interfacial layer. Potassium cations, resulting from charge transfer interactions between the K atoms and the MWNTs

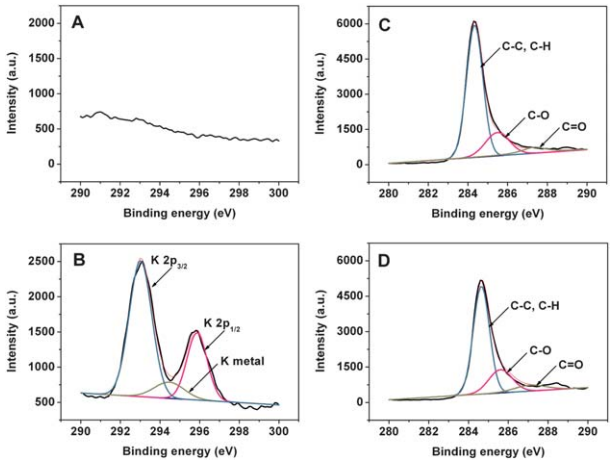

Fig. 1 XPS K 2p spectra of (A) MWNTs and (B) KMWNTs; C 1s spectra of (C) MWNTs and (D) KMWNTs.

backbone may also have contributed in part to this peak component. At higher coverage of K, the K 2p core-level spectrum also reveals the contribution of the metallic K, with the BE for its K $2p_{3/2}$ peak component lying at about 294.4 eV.[49,50] The result is in agreement with intercalation by substitution, which is based on an ion transfer rather than on an electron transfer, as is shown to happen in intercalation by reduction.[33,51] Moreover, such doped K species would decorate the MWNTs and introduce a change in the Fermi level and charge transfer, engendering doping effects, opening the band gap and increasing the conductivity of MWNTs.[52] Therefore, K doping might play an important role in regulating the electronic properties and further enhancing the electrocatalytic activity of MWNTs in electrochemical systems. The K-doping concentration is 8.65 at% in the MWNTs, which is much higher than those of DWNTs (3.2 at%) and SWNTs (0.12 at%).[33,53]

On the other hand, XPS of C 1s ranging from 280 to 290 eV is shown in Fig. 1C and D. Generally, there are several different C groups in pretreated MWNTs, which are characterized by the appearance of several spectral peaks: C–C and C–H at 284.6 eV, C–O at 285.9 eV and C=O at 287.3 eV. The C 1s strong peak at 284.6 eV, which is consistent with sp^2 graphite carbon, did not significantly change, but the at% of C 1s of the KMWNTs decreased compared with that of the undoped MWNTs. Additionally, the intensity peaks characteristic of the C=O groups increased, but those characteristic of C–C decreased, indicating that doping not only introduced K into host MWNTs but also increased the content of oxygen. From the XPS spectra of O 1s before and after K doping (Fig. 2A and B) (C–O at 533.9 eV, C=O at 532.5 eV, and O–C=O at 531.6 eV[54,55]), we can see, after K doping, the oxygen content was 23.47 at%, which is higher than the undoped MWNTs (10.07 at%). This also indicates that the K-doping exhibits a strong charge transfer interaction with carbon atoms and the oxygen atoms.

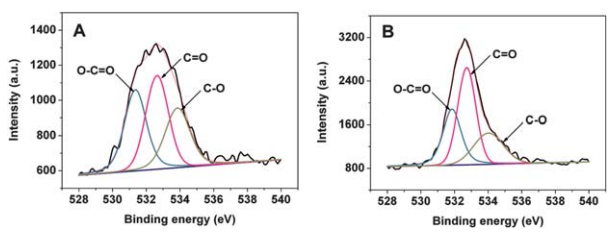

Fig. 2 XPS O 1s spectra of (A) MWNTs and (B) KMWNTs.

KMWNTs gels of RILs, which may be called "bucky gels of ionic liquids", with a wide range of potential applications as a component, can be prepared readily. Typically, when a suspension of KMWNTs in $[BMIM][PF_6]$ was ground with an agate mortar and centrifuged, a transparent liquid phase, identified as pure $[BMIM][PF_6]$, was separated from a black gel phase containing both $[BMIM][PF_6]$ and KMWNTs. The black phase was highly viscous and did not drop when the centrifuge capsule was turned upside down (Fig. 3). As the amount of $[BMIM][PF_6]$ increased, the colorless upper phase increased in volume, while the quantity of the lower black phase (gel phase) remained almost unchanged. When the amount of $[BMIM][PF_6]$ in the starting suspension was smaller than 0.2 mL, no ionic liquid phase separated even upon prolonged centrifugation. The gel phase was estimated to entrap up to 4.45×10^{20} molten salt molecules per 1 mg of KMWNTs (1 wt%).

Fig. 4 shows high-magnification transmission electron microscope (TEM) images of chemically synthesized KMWNTs and KMWNTs–$[BMIM]PF_6$ composite gels. As can be seen from Fig. 4A, there are some defects on the outer wall of the as-synthesized KMWNTs with a diameter of about 10 nm, resulting in rugged graphene sheets. It has previously been reported that the doping of metal ions depends directly on the structural order and morphologies of MWNTs. Indeed, MWNTs with a diameter of 14 nm (40-layer walls) did not react with intercalation, while those with a diameter of 5 nm (4-layer walls) reacted strongly with intercalation, resulting in the formation of nanoflakes, due to the breaking up of the tubes.[32,33,56] In our case, the MWNTs have a diameter of about 10 nm (9-layer walls). Therefore, some disruption at the outer walls of the tubes could be frequently observed, but scarcely any evidence of severance was found along the tube axis. In Fig. 4B, TEM microscopy revealed that the heavily entangled KMWNTs bundles, upon grinding in ionic liquid, are exfoliated to give very ordered bundles, suggesting the KMWNTs were dispersed in the $[BMIM][PF_6]$ to form a homogeneous gel.

The Raman spectrum of the MWNTs (curve a, Fig. 5) shows the characteristic MWNTs peaks at around 1355 cm^{-1}, which is related to the disorder mode (D-band), and at around 1595 cm^{-1}, which presents the tangential modes (G-band). Compared with the MWNTs, the relatively increased intensity of the disorder

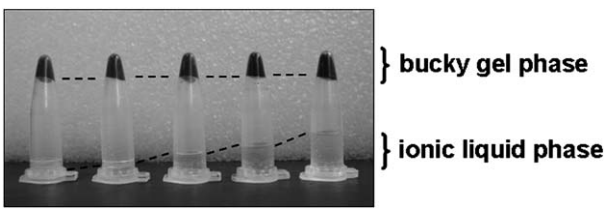

Fig. 3 Pictures of the phase-separation behavior of a bucky gel of $[BMIM][PF_6]$: 2 mg of KMWNTs was ground with 0.2, 0.4, 0.6, 0.8, and 1.0 mL (left-to-right) of $[BMIM][PF_6]$ for 15 min, and the resulting black pastes were centrifuged.

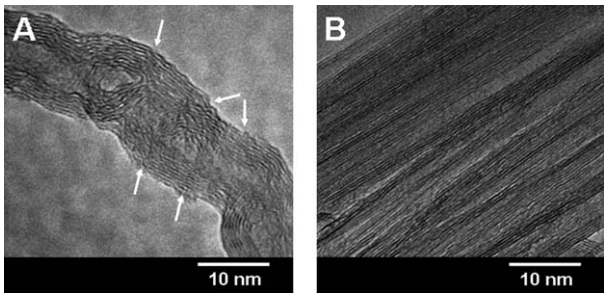

Fig. 4 High magnification TEM images of (A) KMWNTs and (B) KMWNTs–[BMIM]PF_6 composite gels.

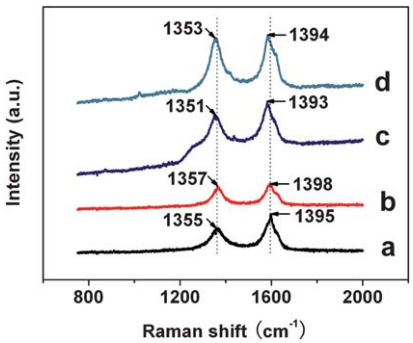

Fig. 5 Raman spectra of (a) MWNTs, (b) KMWNTs, (c) MWNTs–[BMIM]PF_6 and (d) KMWNTs–[BMIM]PF_6.

mode is diagnostic of disruptions in the hexagonal framework of MWNTs.[57,58] The Raman spectrum of the KMWNTs showed a disorder-induced D band at $\lambda = 1357$ cm^{-1} and a tangential stretch G band at $\lambda = 1598$ cm^{-1} (curve b, Fig. 5), with an intensity ratio $I_D/I_G = 0.93$. This value was much higher than the 0.47 for the MWNTs, indicating that K-doping was very effective in introducing defects into the structure of the MWNTs. In comparison with MWNTs, the D and G bands of MWNTs–[BMIM]PF_6 slightly shifted to $\lambda = 1351$ and 1593 cm^{-1} (curve c, Fig. 5), respectively, which could be associated with [BMIM]PF_6 bound to the MWNTs. Moreover, the values of I_D/I_G for the MWNTs and MWNTs–[BMIM]PF_6 did not show obvious differences, thus indicating that the functionalization of MWNTs with [BMIM]PF_6 did not destroy the structure of the MWNTs. Similarly, the D and G bands of KMWNTs–[BMIM]PF_6 slightly shifted to $\lambda = 1353$ and 1594 cm^{-1} (curve d, Fig. 5), respectively. The values of I_D/I_G for the KMWNTs and KMWNTs–[BMIM]PF_6 remain unchanged upon gelation. From these spectral profiles, we conclude that the gelation is triggered only physically, without chemical denaturation of MWNTs or KMWNTs.

To investigate the effect of the KMWNTs–[BMIM]PF_6 composite film on the electron transfer kinetics of the redox probe at the electrode interface, cyclic voltammograms of the KMWNTs–[BMIM]PF_6/GCE in 0.1 M KCl solution containing 5 mM $K_3[Fe(CN)_6]/K_4[Fe(CN)_6]$ are shown in curve e, Fig. 6. The peak currents greatly increased compared with those of the MWNTs–[BMIM]PF_6/GCE (curve d, Fig. 6), KMWNTs/GCE (curve c, Fig. 6), MWNTs/GCE (curve b, Fig. 6) and bare GCE (curve a, Fig. 6). The potential differences of the peak-to-peak

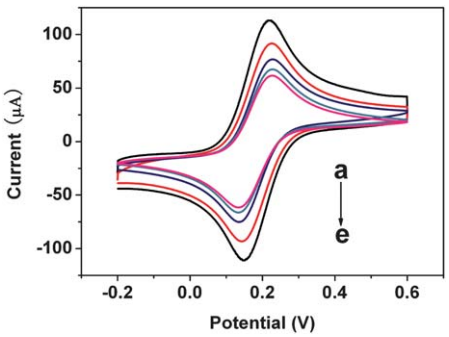

Fig. 6 Cyclic voltammograms of (a) the bare GCE, (b) the MWNTs/GCE, (c) the KMWNTs/GCE, (d) the MWNTs–[BMIM]PF_6/GCE and (e) the KMWNTs–[BMIM]PF_6/GCE in 0.1 M KCl solution containing 5 mM $K_3[Fe(CN)_6]/K_4[Fe(CN)_6]$. Scan rate: 50 mV s^{-1}.

(D_{EP}) at the KMWNTs–[BMIM]PF_6/GCE, MWNTs–[BMIM]PF_6/GCE, KMWNTs/GCE, MWNTs/GCE and bare GCE are 82, 85, 90, 92 and 93 mV, respectively. Both the small differences between these D_{EP} and the changes in peak currents showed that the KMWNTs–[BMIM]PF_6 composite gels effectively accelerate the electron transfer between $Fe(CN)_6^{3-/4-}$ and the electrode.

Electrocatalytic reduction of dissolved oxygen

A comparison of the electrocatalytic reduction of oxygen at different electrodes in air-saturated 0.1 M pH 7.4 PBS with the potential range from +0.2 to −0.8 V is shown in Fig. 7. The reduction current of dissolved oxygen increased with the order of bare GCE < [BMIM]PF_6/GCE < MWNTs/GCE < KMWNTs/GCE < MWNTs–[BMIM]PF_6/GCE < KMWNTs–[BMIM]PF_6/GCE. The electrocatalytic reduction peak potentials both shifted positively to *ca.* −0.30 V at the MWNTs–[BMIM]PF_6/GCE (curve e, Fig. 7) and KMWNTs–[BMIM]PF_6/GCE (curve f, Fig. 7). The peak current at the KMWNTs–[BMIM]PF_6/GCE is much higher than those of others. Moreover, the KMWNTs–[BMIM]PF_6 modified electrode showed no obvious reduction peak in nitrogen-saturated PBS (curve a, inset of Fig. 7), whereas

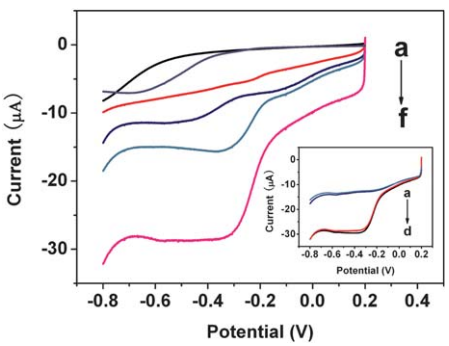

Fig. 7 (A) LSV for the oxygen reduction at (a) the bare/GCE, (b) the [BMIM]PF_6/GCE, (c) the MWNTs/GCE, (d) the KMWNTs/GCE, (e) the MWNTs–[BMIM]PF_6/GCE and (f) the KMWNTs–[BMIM]PF_6/GCE recorded in air-saturated 0.1 M pH 7.4 PBS. Inset: LSV of the KMWNTs–[BMIM]PF_6/GCE in 0.1 M pH 7.4 nitrogen-saturated PBS (a), nitrogen-saturated PBS containing 0.264 mM H_2O_2 (b), air-saturated PBS (c) and air-saturated PBS containing 0.264 mM H_2O_2 (d).

a great increase of the reduction peak current was observed in air-saturated PBS (curve c, inset of Fig. 7). Additionally, the saturated concentration of dissolved oxygen in water was 0.264 mM. When the same concentration of H_2O_2 was added to nitrogen-saturated (curve b, inset of Fig. 7) and air-saturated PBS (curve d, inset of Fig. 7) at the KMWNTs–$[BMIM]PF_6$/GCE, respectively, the linear sweep voltammograms have no obvious change between curve a and b and curve c and d in the potential range from −0.8 to +0.2 V, indicating the KMWNTs–$[BMIM]PF_6$ modified electrode is insensitive to H_2O_2. Clearly, the electrocatalytic reduction of oxygen at the KMWNTs–$[BMIM]PF_6$/GCE showed a synergic effect of KMWNTs and $[BMIM]PF_6$ which possessed superior electrocatalytic ability for the reduction of dissolved oxygen.

The corresponding calibration curves for the detection of oxygen in nitrogen-saturated PBS with successive addition of varying concentrations of air-saturated PBS at different electrodes are shown in Fig. 8. The sensitivity of the KMWNTs–$[BMIM]PF_6$/GCE to the reduction of dissolved oxygen was 156.7 μA mM^{-1} (curve e, Fig. 8), which was larger than those of 57.8, 17.8 and 11.6 μA mM^{-1}, respectively, for the MWNTs–$[BMIM]PF_6$/GCE (curve d, Fig. 8), KMWNTs/GCE (curve c, Fig. 8) and MWNTs/GCE (curve b, Fig. 8) at −0.3 V for the reduction of dissolved oxygen. Almost no electrochemical response was observed at the bare/GCE (curve a, Fig. 8). The linear response range of the KMWNTs–$[BMIM]PF_6$/GCE to oxygen concentration was from 0.0264 to 39.4 μM ($R = 0.999$). The detection limit was 0.01 μM (S/N = 3). Hence, the as-prepared KMWNTs–$[BMIM]PF_6$ composite gels could be a promising material for $O_2^{\cdot-}$ sensing.

Analytical performances of the KMWNTs–$[BMIM]PF_6$–SOD/GCE

KMWNTs–$[BMIM]PF_6$ composite gels offer a markedly decreased overvoltage for the dissolved oxygen reduction to allow low-overpotential amprometric measurement. This is of considerable interest to the operation of oxidase-based amperometric biosensors because oxygen will be produced during the enzyme/superoxide reaction. With the addition of $O_2^{\cdot-}$, the SOD can chemically catalyze the oxidation of $O_2^{\cdot-}$ to O_2 and H_2O_2. As a result, the concentration of $O_2^{\cdot-}$ can be indirectly detected by the determination of the liberated oxygen in the reaction.

Fig. 9 displays the amperometric response of the KMWNTs–$[BMIM]PF_6$–SOD/GCE with the successive addition of deoxygenated KO_2 solution to 0.1 M pH 7.4 PBS at −0.3 V. When KO_2 is added to the nitrogen-saturated buffer solution, the reduction current rises steeply to achieve 95% of the steady current in less than 3 s. Additionally, no obvious detection signal can be observed at the KMWNTs–$[BMIM]PF_6$/GCE (free of SOD) with the addition of deoxygenated KO_2 solution. This suggests that the amperometric response of the KMWNTs–$[BMIM]PF_6$–SOD/GCE upon the addition of KO_2 is ascribed to the O_2 produced during the enzyme/superoxide reaction.

The linear response range of the KMWNTs–$[BMIM]PF_6$–SOD/GCE to $O_2^{\cdot-}$ concentration was from 0.04 to 38 μM ($R = 0.998$) (inset A of Fig. 9). The detection limit was 0.024 μM (S/N = 3). The sensitivity of the KMWNTs–$[BMIM]PF_6$–SOD/GCE for the detection of $O_2^{\cdot-}$ was 98.2 μA mM^{-1}, which was much larger than those of 17.1 ± 0.4 μA mM^{-1} for ZnO

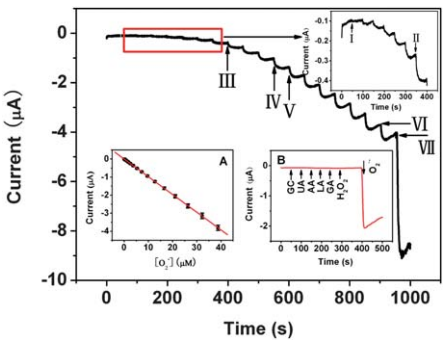

Fig. 9 A current–time curve of the KMWNT-$[BMIM]PF_6$–SOD/GCE with the successive addition of deoxygenated KO_2 (indicated by arrows for marked concentrations: $c = 0.04n$ μM, I → II, $n = 1, 2, 4, 8, 16, 18, 20$; III → IV, $n = 30, 40, 50, 60$; V → VI, $n = 80, 100, 120, 140, 160, 180, 200$; VII, $n = 2000$) in a stirred 0.1 M pH 7.4 nitrogen-saturated PBS at −0.3 V. Inset: (A) a calibration plot illustrating the linear electrode response to KO_2 addition; (B) the selectivity profile of the KMWNTs–$[BMIM]PF_6$–SOD/GCE over interfering species of GC (5 mM), UA (0.1 mM), AA (0.1 mM), LA (0.1 mM), GA (0.1 mM) and H_2O_2 (0.2 mM) as well as $O_2^{\cdot-}$ (20 μM) at −0.3 V.

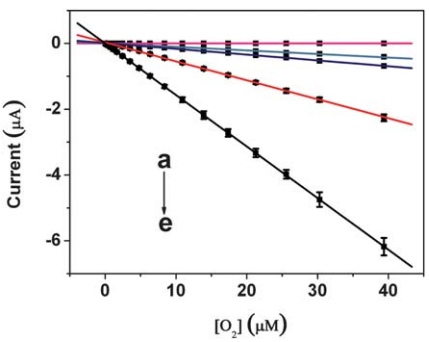

Fig. 8 Calibration plots of (a) the bare/GCE, (b) the MWNTs/GCE, (c) the KMWNTs/GCE, (d) the MWNTs–$[BMIM]PF_6$/GCE and (e) the KMWNTs–$[BMIM]PF_6$/GCE against the concentration of O_2. Applied potential: −0.3 V.

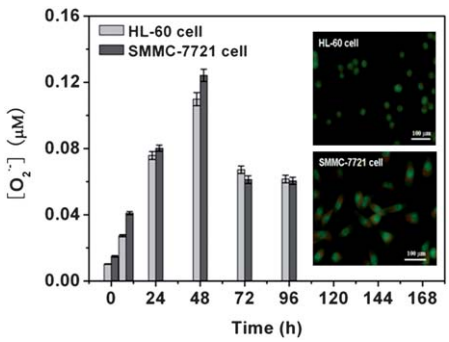

Fig. 10 The time-dependent concentration of $O_2^{\cdot-}$ released from HL-60 and SMMC-7721cells (10^5 cells cm^{-2}) after treatment with 50 ng mL^{-1} LPS. The insets show images of HL-60 and 7721cells (48 h) recorded with a DMIRE2 inverted fluorescence microscope.

Table 1 Recovery measurements of $O_2^{\cdot-}$ released from HL-60 and SMMC-7721cells (10^5 cells cm^{-2}) using the developed method

Sample no.	Added amounts (μM)	Measured amounts (μM)[a]	Recovery (%)	RSD (%)
HL-60 cell	0.2	0.196	98.0	3.04
	0.3	0.307	102.3	
	0.6	0.611	101.8	
SMMC-7721 cell	0.2	0.202	101	3.33
	0.3	0.305	101.7	
	0.6	0.617	102.8	

[a] Values determined from the KMWNTs–[BMIM]PF_6–SOD/GCE; an average value of the response of five measurements is shown for each sample.

nanodisks and 12.4 μA mM^{-1} for nickel oxide modified electrodes.[9,59] The stability of the KMWNTs–[BMIM]PF_6–SOD/GCE was examined in 0.1 M pH 7.4 PBS with 10 μM $O_2^{\cdot-}$ at −0.3 V. The relative standard deviation (RSD) was 2.9% for five successive measurements. The fabrication reproducibility of five electrodes, made independently, showed an acceptable reproducibility with a RSD of 3.4% for the current signal of 10 μM $O_2^{\cdot-}$. Moreover, the electrodes were stored in 0.1 M pH 7.0 PBS at 4 °C in a refrigerator with periodical measurements, and they remained stable during the first week. After one month, the biosensors still retained 80% of the initial sensitivity, which is due to the good durability and biocompatibility of the KMWNTs–[BMIM]PF_6 composite gels, thus providing a perfect microenvironment for SOD to retain its bioactivity.

In real samples, there are some coexisting electroactive species such as glucose (GC), UA, AA, lactic acid (LA), glutamic acid (GA), *etc.* that might affect the biosensor's response. The selectivity and anti-interference advantages of the biosensor are demonstrated (inset B of Fig. 9). A well-defined $O_2^{\cdot-}$ response is observed at the biosensor, whereas relevant physiological levels of UA, AA, LA, GA (0.1 mM), and GC (5 mM) result in negligible signals. Additionally, in biological systems, H_2O_2 is a metabolite in the degradation of $O_2^{\cdot-}$ and a product of enzyme reactions of endogenous oxidase such as monoamine oxidase and L-amino acid oxidase. Moreover, H_2O_2 is one of the main byproducts in the enzyme-catalytic system which can catalyze $O_2^{\cdot-}$ to generate O_2. Therefore, the specificity of the sensor against H_2O_2 is of great importance in its application for the determination of $O_2^{\cdot-}$ in biological systems as well as in its calibration. Thus, the interference from H_2O_2 was also examined (inset B of Fig. 9). As shown, no current response was observed for 0.2 mM H_2O_2. Therefore, a highly selective response to $O_2^{\cdot-}$ is obtained without the use of a perm-selective membrane or enzymatic preoxidation.

Determination of $O_2^{\cdot-}$ released from HL-60 and SMMC-7721 cancer cells

To evaluate its applicability, the biosensor was used for the determination of the concentrations of $O_2^{\cdot-}$ released from HL-60 and SMMC-7721 cancer cells. The results indicated that the $O_2^{\cdot-}$ concentrations from HL-60 and SMMC-7721 cells (10^5 cells cm^{-2}) are *ca.* 0.01 and 0.015 μM (Fig. 10), respectively, which are in agreement with the previous report that the physiological concentration of $O_2^{\cdot-}$ is in the range of 10^{-8} M.[9] The developed method was also used to measure $O_2^{\cdot-}$ released from lipopolysaccharide (LPS) treated HL-60 and SMMC-7721 cells. Fig. 10 depicts the time course experimental results with LPS loading. The values of $O_2^{\cdot-}$ from HL-60 and SMMC-7721 cells are significantly increased after treatment with 50 ng mL^{-1} LPS for 8 h, and reach the highest values (*ca.* 0.12 μM) at 48 h, as reported in the literature.[17] Afterwards, the concentrations decrease gradually and reach relatively stable values (*ca.* 0.06 μM). Therefore, the proposed method could be used to study the cellular kinetics of $O_2^{\cdot-}$.

To evaluate the precision of the $O_2^{\cdot-}$ concentrations produced by HL-60 and SMMC-7721 cells detected with the developed method, recovery measurements were carried out. After 48 h stimulation by LPS, two samples from HL-60 and SMMC-7721 cells with different concentrations were prepared, and certain amounts of $O_2^{\cdot-}$ were added. The results are presented in Table 1. The average recoveries for the two different samples are 100.7% and 101.8%, respectively, and the RSD are 3.04 and 3.33%, respectively, indicating that the developed approach has high accuracy in measuring $O_2^{\cdot-}$ concentrations released from HL-60 and SMMC-7721 cells. These observations substantially demonstrate that the developed method represents a new biosensing platform for reliable determination of $O_2^{\cdot-}$ *in vitro* and from cancer cells and could be potentially useful for further physiological and pathological studies.

Conclusions

A novel composite material made from mixing KMWNTs with a RIL ([BMIM][PF_6]) has been designed to construct a highly specific biosensor for selective measurement of $O_2^{\cdot-}$. The KMWNTs–[BMIM]PF_6 composite gels showed good dispersion of KMWNTs in [BMIM]PF_6 by "cation–π" interactions. The presence of KMWNTs and [BMIM]PF_6 produces a synergic effect that accelerates the electron transfer between the redox probe and the electrode. More importantly, the KMWNTs–[BMIM]PF_6 modified electrode showed a marked electrocatalytic activity toward oxygen reduction in neutral solution. Therefore, the composite film can be used for monitoring oxygen and further constructing $O_2^{\cdot-}$ biosensors. This is of great advantage in the measurement of $O_2^{\cdot-}$, especially in biological systems, due to the KMWNTs–[BMIM]PF_6 composite gels having a high specificity against AA, UA, H_2O_2, and metabolites of some neurotransmitters. The obtained results demonstrate that the present sensor is very promising for the durable and reliable measurement of $O_2^{\cdot-}$ *in vitro* and from cancer cells, such as liver cancer and leukemia cells. This work is anticipated to open a new possibility in the investigation of KMWNTs composite gels of imidazolium ion-based ionic liquids and

promote their application in biosensor construction for the highly selective measurement of $O_2^{\cdot-}$ in biological systems.

Acknowledgements

The work was financially supported by the 973 Program (Grant Number 2012CB932600), the National Natural Science Funds (Grant Number 21025522, 21135003 and 20890021), the National Natural Science Funds for Creative Research Groups (Grant Number 20821063) of China and the academic leaders cultivation program for outstanding middle aged and young personnel of Nanjing University, China.

Notes and references

1 B. Halliwell and J. M. C. Gutteridge, *Free Radicals in Biology and Medicine*, Oxford University Press, Oxford, UK, 3rd edn, 1999.
2 H. A. Kontos and E. P. Wei, *J. Neurosurg.*, 1986, **64**, 803–807.
3 M. Y. Globus, O. Alonso, W. A. Dietrich, R. Busto and M. D. Ginsberg, *J. Neurochem.*, 1995, **65**, 1704–1711.
4 Y. Tian, L. Q. Mao, T. Okajima and T. Ohsaka, *Anal. Chem.*, 2002, **74**, 2428–2434.
5 E. D. Hall and J. M. Braughler, *Free Radical Biol. Med.*, 1989, **6**, 303–313.
6 A. Vanella, C. Di Giacomo, V. Sorrenti, A. Russo, C. Castorina, A. Campisi, M. Renis and J. R. Perez-Polo, *Neurochem. Res.*, 1993, **18**, 1337–1340.
7 R. A. Floyd, *FASEB J.*, 1990, **4**, 2587–2597.
8 B. N. Ames, M. K. Shigenaga and T. M. Hagen, *Proc. Natl. Acad. Sci. U. S. A.*, 1993, **90**, 7915–7922.
9 Z. F. Deng, Q. Rui, X. Yin, H. Q. Liu and Y. Tian, *Anal. Chem.*, 2008, **80**, 5839–5846.
10 Y. P. Luo, H. Q. Liu, Q. Rui and Y. Tian, *Anal. Chem.*, 2009, **81**, 3035–3041.
11 B. Halliwell, *J. Neurochem.*, 1992, **59**, 1609–1623.
12 G. Benzi and A. Moretti, *Free Radical Biol. Med.*, 1995, **19**, 77–101.
13 S. J. Stohs and D. Bagchi, *Free Radical Biol. Med.*, 1995, **18**, 321–336.
14 J. S. Beckman and W. H. Kippenol, *Am. J. Physiol.*, 1995, **271**, 1424–1437.
15 S. S. Gross and M. S. Wolin, *Annu. Rev. Physiol.*, 1995, **57**, 737–769.
16 V. Lvovich and A. Scheeline, *Anal. Chem.*, 1997, **69**, 454–462.
17 S. Rajesh, A. K. Kanugula, K. Bhargava, G. Ilavazhagan, S. Kotamraju and C. Karunakaran, *Biosens. Bioelectron.*, 2010, **26**, 689–695.
18 A. A. Abdelwahab, W. C. A. Koh, H. B. Noh and Y. B. Shim, *Biosens. Bioelectron.*, 2010, **26**, 1080–1086.
19 S. Mesaros, Z. Vankova, A. Mesarosova, P. Tomcik and S. Grunfeld, *Bioelectrochem. Bioenerg.*, 1998, **46**, 33–37.
20 S. Descroix and F. Bedioui, *Electroanalysis*, 2001, **13**, 524–528.
21 C. J. McNeil, K. R. Greenough, P. A. Weeks, C. H. Self and J. M. Cooper, *Free Radical Res.*, 1992, **17**, 399–406.
22 P. Manning, C. J. McNei, J. M. Cooper and E. W. Hillhouse, *Free Radical Biol. Med.*, 1998, **24**, 1304–1309.
23 M. I. Song, F. F. Bier and F. W. Scheller, *Bioelectrochem. Bioenerg.*, 1995, **38**, 419–422.
24 V. Lvovich and A. Scheeline, *Anal. Chim. Acta*, 1997, **354**, 315–323.
25 L. Campanella, A. Bonanni, G. Favero and M. Tomassetti, *Anal. Bioanal. Chem.*, 2003, **375**, 1011–1016.
26 S. Descroix and F. Bedioui, *Electroanalysis*, 2001, **13**, 524–528.
27 S. Mesaros, Z. Vankova, S. Grunfeld, A. Mesarosova and T. Malinski, *Anal. Chim. Acta*, 1998, **358**, 27–31.
28 P. Pernot, J. P. Mothet, O. Schuvailo, A. Soldatkin, L. Pollegioni, M. Pilone, M. T. Adeline, R. Cespuglio and S. Marinesco, *Anal. Chem.*, 2008, **80**, 1589–1597.
29 Y. Wang, Y. Y. Shao, D. W. Matson, J. H. Li and Y. H. Lin, *ACS Nano*, 2010, **4**, 1790–1798.
30 Y. C. Ma, A. S. Foster, A. V. Krasheninnikov and R. M. Nieminen, *Phys. Rev. B*, 2005, **72**, 205416-1–205416-6.
31 C. W. Zhou, J. Kong, E. Yenilmez and H. J. Dai, *Science*, 2000, **290**, 1552–1555.
32 K. Y. Chun, S. K. Choi, H. J. Kang, C. Y. Park and C. J. Lee, *Carbon*, 2006, **44**, 1491–1495.
33 K. Y. Chun and C. J. Lee, *J. Phys. Chem. C*, 2008, **112**, 4492–4497.
34 C. Y. Deng, J. H. Chen, X. L. Chen, C. H. Xiao, L. H. Nie and S. Z. Yao, *Biosens. Bioelectron.*, 2008, **23**, 1272–1277.
35 J. C. Carrero-Sánchez, A. L. Elías, R. Mancilla, G. Arrellín, H. Terrones, J. P. Laclette and M. Terrones, *Nano Lett.*, 2006, **6**, 1609–1616.
36 C. L. Sun, H. W. Wang, M. Hayashi, L. C. Chen and K. H. Chen, *J. Am. Chem. Soc.*, 2006, **128**, 8368–8369.
37 R. Sen, B. C. Satishkumar, A. Govindaraj, K. R. Harikumar, M. K. Renganathan and C. N. R. Rao, *J. Mater. Chem.*, 1997, **7**, 2335–2337.
38 B. G. Sumpter, V. Meunier, J. M. Romo-Herrera, E. Cruz-Silva, D. A. Cullen, H. Terrones, D. J. Smith and M. Terrones, *ACS Nano*, 2007, **1**, 369–375.
39 X. Xu, S. J. Jiang, Z. Hu and S. Q. Liu, *ACS Nano*, 2010, **4**, 4292–4298.
40 J. Campos-Delgado, I. O. Maciel, D. A. Cullen, D. J. Smith, A. Jorio, M. A. Pimenta, H. Terrones and M. Terrones, *ACS Nano*, 2010, **4**, 1696–1702.
41 R. S. Lee, H. J. Kim, J. E. Fischer, A. Thess and R. E. Smalley, *Nature*, 1997, **388**, 255–257.
42 T. Fukushima, A. Kosaka, Y. Ishimura, T. Yamamoto, T. Takigawa, N. Ishii and T. Aida, *Science*, 2003, **300**, 2072–2074.
43 J. C. Ma and D. A. Dougherty, *Chem. Rev.*, 1997, **97**, 1303–1324.
44 T. Welton, *Chem. Rev.*, 1999, **99**, 2071–2083.
45 P. Wasserscheid and W. Keim, *Angew. Chem., Int. Ed.*, 2000, **39**, 3772–3789.
46 J. G. Huddleston, A. E. Visser, W. M. Reichert, H. D. Willauer, G. A. Broker and R. D. Rogers, *Green Chem.*, 2001, **3**, 156–164.
47 K. R. Seddon, *J. Chem. Technol. Biotechnol.*, 1997, **68**, 351–356.
48 V. R. Koch, C. Nanjundiah and R. T. Carlin, Covalent Associates Incorporated, U. S. Patent 5827602, 1998.
49 J. F. Moulder, W. F. Stickle, P. E. Sobol and K. D. Bomben, *Handbook of X-ray Photoelectron Spectroscopy*, Perkin Elmer, Eden Prairie, MN, 1992.
50 S. Li, E. T. Kang, K. G. Neoh, Z. H. Ma, K. L. Tan and W. Huang, *Appl. Surf. Sci.*, 2001, **181**, 201–210.
51 R. Clement, in *Hybrid Organic-Inorganic Composites*, ed. J. E. Mark, C. Y. C. Lee and P. A. Bianconi, ACS Symposium Series, No. 585, American Chemical Society, Washington, DC, 1995.
52 C. Jo, C. Kim and Y. H. Lee, *Phys. Rev. B: Condens. Matter*, 2002, **65**, 035420-1–035420-5.
53 B. Ha and C. J. Lee, *Appl. Phys. Lett.*, 2007, **90**, 023108-1–023108-3.
54 P. Y. Brisson, H. Darmstadt, M. Fafard, A. Adnot, G. Servant and G. Soucy, *Carbon*, 2006, **44**, 1438–1447.
55 Y. Wang, Y. Y. Shao, D. W. Matson, J. H. Li and Y. H. Lin, *ACS Nano*, 2010, **4**, 1790–1798.
56 V. Z. Mordkovitch, *Mol. Cryst. Liq. Cryst. Sci. Technol., Sect. A*, 2000, **340**, 775–780.
57 Y. J. Zhang, J. Li, Y. F. Shen, M. J. Wang and J. H. Li, *J. Phys. Chem. B*, 2004, **108**, 15343–15346.
58 X. Zhong, H. J. Bai, J. J. Xu, H. Y. Chen and Y. H. Zhu, *Adv. Funct. Mater.*, 2010, **20**, 992–999.
59 A. Salimi, A. Noorbakhsh, H. A. Rafiee-Pour and H. Ghourchian, *Electroanalysis*, 2011, **23**, 683–691.